

Abdominal DCE-MRI reconstruction with deformable motion correction for liver perfusion quantification

Adam Johansson^{a)}

Department of Radiation Oncology, University of Michigan, Ann Arbor, MI 48109, USA

James M. Balter

Department of Radiation Oncology, University of Michigan, Ann Arbor, MI 48109, USA

Department of Biomedical Engineering, University of Michigan, Ann Arbor, MI 48109, USA

Yue Cao

Department of Radiation Oncology, University of Michigan, Ann Arbor, MI 48109, USA

Department of Radiology, University of Michigan, Ann Arbor, MI 48109, USA

Department of Biomedical Engineering, University of Michigan, Ann Arbor, MI 48109, USA

(Received 18 March 2018; revised 29 July 2018; accepted for publication 29 July 2018; published 31 August 2018)

Purpose: Abdominal dynamic contrast-enhanced (DCE) MRI suffers from motion-induced artifacts that can blur images and distort contrast-agent uptake curves. For liver perfusion analysis, image reconstruction with rigid-body motion correction (RMC) can restore distorted portal-venous input functions (PVIF) to higher peak amplitudes. However, RMC cannot correct for liver deformation during breathing. We present a reconstruction algorithm with deformable motion correction (DMC) that enables correction of breathing-induced deformation in the whole abdomen.

Methods: Raw data from a golden-angle stack-of-stars gradient-echo sequence were collected for 54 DCE-MRI examinations of 31 patients. For each examination, a respiratory motion signal was extracted from the data and used to reconstruct 21 breathing states from inhale to exhale. The states were aligned with deformable image registration to the end-exhale state. Resulting deformation fields were used to correct back-projection images before reconstruction with view sharing. Images with DMC were compared to uncorrected images and images with RMC.

Results: DMC significantly increased the PVIF peak amplitude compared to uncorrected images ($P \ll 0.01$, mean increase: 8%) but not compared to RMC. The increased PVIF peak amplitude significantly decreased estimated portal-venous perfusion in the liver ($P \ll 0.01$, mean decrease: 8 ml/100 ml-min). DMC also removed artifacts in perfusion maps at the liver edge and reduced blurring of liver tumors for some patients.

Conclusions: DCE-MRI reconstruction with DMC can restore motion-distorted uptake curves in the abdomen and remove motion artifacts from reconstructed images and parameter maps but does not significantly improve perfusion quantification in the liver compared to RMC. © 2018 American Association of Physicists in Medicine [<https://doi.org/10.1002/mp.13118>]

Key words: contrast agent, DCE MRI, deformable image registration, liver, motion artifacts, motion correction, MRI, perfusion

Abbreviations

AIF arterial input function

CA contrast agent

DCE MRI dynamic contrast-enhanced MRI

DMC deformable motion correction

FOV field of view

Gd-BOPTA gadobenate dimeglumine

Gd-EOB-DTPA gadolinium ethoxybenzyl diethylenetriamine
pentaacetic acid

GRASP golden-angle radial sparse parallel

GTV gross tumor volume

KWIC k-space weighted image contrast

MR magnetic resonance

NMC no motion correction

NTV normal tissue volume

PET positron emission tomography

PK pharmacokinetic

PVIF portal-venous input function

RMC rigid-body motion correction

ROI region of interest

VIBE volume interpolated breathhold examination

1. INTRODUCTION

Arterial and portal-venous perfusion as well as hepatobiliary uptake can be measured by dynamic contrast-enhanced (DCE) MRI and used to determine local and global liver function as well as lesion extent for patients with liver cancer.^{1–12} Perfusion and uptake maps, derived from DCE MRI, can support individualized adaptive radiotherapy

treatments that maximize sparing of excess irradiation of functional parts of the liver. By sparing function in non-cancerous liver tissue, the probability of treatment complications can be reduced.

However, respiratory, cardiac, and gastrointestinal motion pose challenges for DCE MRI of the abdomen and can introduce streaks and blurring into acquired images. Contrast-agent (CA) uptake curves extracted from dynamic time series can also be corrupted by motion resulting in inaccurate hepatic perfusion or retention estimation.

Breath holds can reduce this problem.⁷ However, not all patients are able to hold their breath for long enough or often enough to allow the CA uptake curves to be faithfully captured. Alternatively, DCE-MRI images can be compensated for motion after reconstruction using image registration.^{13,14} Postreconstruction alignment can compensate for inter-image motion but cannot undo blurring or remove image streaks arising from intra-image motion. Parallel imaging has been applied to increase the temporal resolution of DCE MRI to 1.6–1.9 s¹⁵ to render motion-related blur negligible for slowly breathing subjects. However, patients who breathe faster will still be subject to motion-induced artifacts. Alternatively, a respiratory dimension has been added to the reconstruction such that a dynamic contrast-enhanced time series is reconstructed for each respiratory phase, but this may limit the temporal resolution to 11–12 s, which is not adequate for perfusion analysis.^{16–18}

Instead of aligning images after reconstruction, Lin *et al.* corrected acquired data in k-space and used translational alignment to reduce intra-image artifacts.¹⁹ We previously modified this method to include rotation and investigated its effect on CA uptake curves.²⁰ Rigid-body motion correction was found to restore portal-venous input functions (PVIFs) to higher amplitudes. However, for 13% of subjects, residual deformations larger than 10 mm were found in more than 5% of the liver volume. This finding, suggests that a method of motion-corrected reconstruction, that accommodates liver deformation due to breathing during DCE-MRI acquisition, may be needed.

Reconstruction methods with integrated deformable motion correction have been implemented by several authors using iterative model-based reconstruction^{21,22} to achieve reductions of motion-induced aliasing. A simpler approach has been successfully used for motion correction of positron emission tomography (PET) images from PET/MRI scanners^{23,24} and relies on direct deformation of temporal subimages with negligible intra-frame motion, that are then combined into motion corrected images. While this strategy does not optimally reduce motion-induced aliasing for MRI reconstruction, it can achieve results similar to those from iterative model-based reconstruction,^{21,25} especially if deformation fields are approximately affine within the width of the receiver-coil sensitivities.²⁶ This simplified strategy can also shorten reconstruction times to a fraction of what is needed for model-based reconstruction²¹, which is important to achieve impact in the radiation therapy clinic.

In this work, we present a DCE-MRI reconstruction algorithm with integrated deformable motion correction and

apply it to a golden-angle stack-of-stars gradient-echo MR sequence. The algorithm uses deformation of back-projection images, building upon motion-correction strategies previously used for PET images from PET/MRI scanners^{23,24} and for MRI images.²⁶ CA uptake curves and perfusion maps derived from images with deformable and rigid-body motion correction as well as images without motion correction are compared and the effects of motion correction on artifacts in perfusion maps and on lesions are presented.

2. MATERIALS AND METHODS

2.A. Imaging

Under institutional review board approval, 54 DCE-MRI examinations of 31 patients (women, 11; men, 20; age at examination, 48–78 yr; number of examinations per patient, 1–3) were performed as part of a pilot study of individualized adaptive radiation therapy for hepatocellular carcinoma. A 3-T MRI scanner (Magnetom Skyra, Siemens Healthineers, Erlangen, Germany) was used. As part of the scan protocol, a 5-min DCE-MRI scan was performed using a work-in-progress golden-angle stack-of-stars spoiled gradient echo sequence^{27,28} with fat suppression. A 20 ml (0.5 M) of Gd-BOPTA (MultiHance, Bracco Diagnostics, Monroe, NJ) was administered 30 s after the start of scanning. For reception, an 18-channel flexible surface coil (Body Matrix) was used in combination with 2–5 elements of the posterior coils built into the scanner table (Spine Matrix). Sequence parameters are listed in Table I. Images reconstructed by vendor software, using k-space weighted image contrast (KWIC)²⁹ without motion correction, as well as raw k-space data were collected after each examination. The temporal spacing between the vendor-reconstructed image volumes was 3.3–5.4 s.

Aside from the vendor-reconstructed time series, images were reconstructed using a view-sharing algorithm with and without motion correction. The flowchart in Fig. 1 illustrates the motion-correction and reconstruction pipeline used to process the collected data into DCE-MRI image time series.

TABLE I. DCE-MRI sequence parameters.

Sequence parameter	
Sequence type	Golden-angle stack-of-stars spoiled gradient echo with fat suppression
Echo time	1.14–1.21 ms
Repetition time	2.72–4.51 ms
Flip angle	10°–14°
Image matrix size	192 × 192
Number of slices	64
Number of partitions	46
Number of radial spokes	2000
In-plane voxel size	2–2.45 mm
Slice thickness	3–4 mm

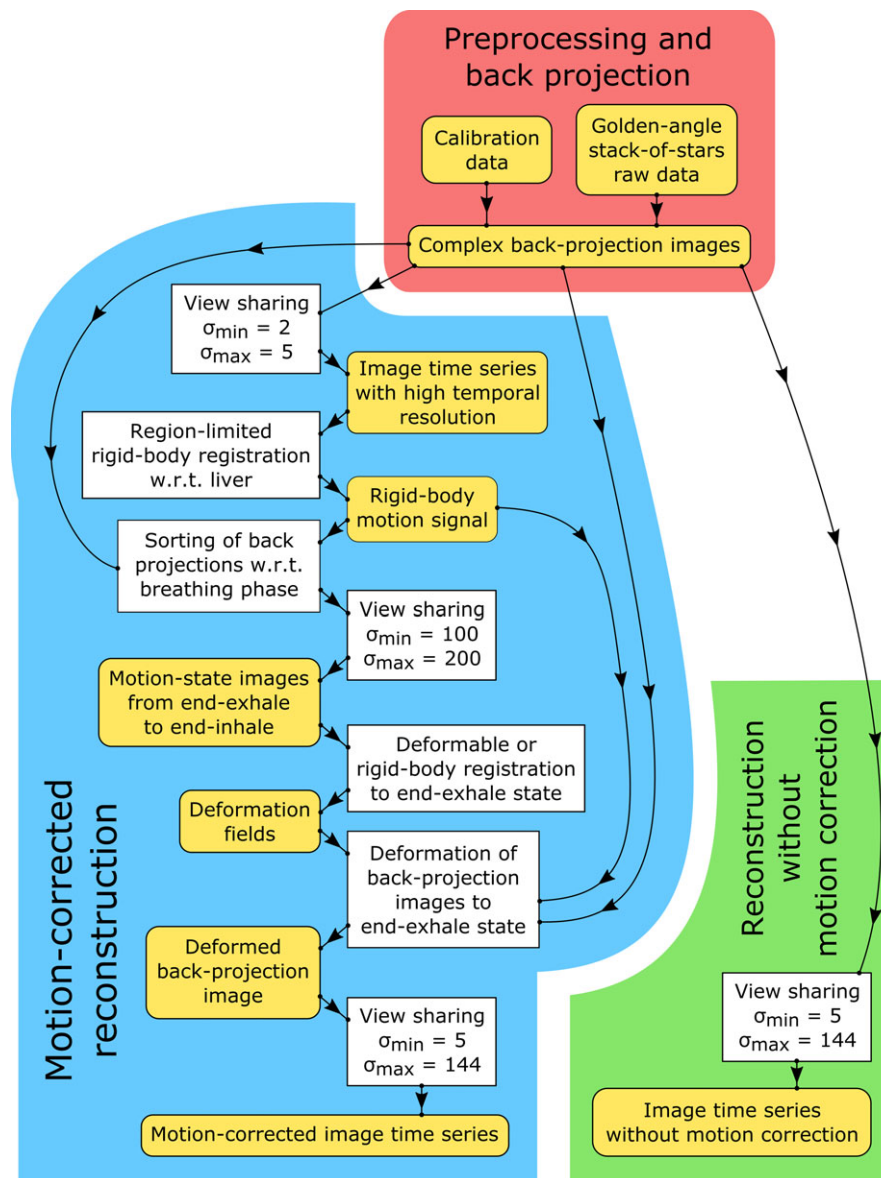


FIG. 1. Overview of the reconstruction and motion-correction pipeline. Yellow rounded boxes represent pieces of data and white unrounded boxes represent processing steps. The blue box contains steps that perform motion-corrected reconstruction. The red field contains preprocessing steps and the green contains steps for reconstruction without motion correction. The parameters σ_{\min} and σ_{\max} describe the minimum and maximum width of the view-sharing filter. [Color figure can be viewed at wileyonlinelibrary.com]

The different parts of the pipeline are described in detail below.

2.B. Data collection and adjustments

Prior to scanning, a calibration scan was used to determine a receiver-coil noise whitening transform³⁰ as well as a set of coil sensitivities.³¹ After calibration, subjects were scanned with 2000 radial through-center spokes. Imaging parameters are summarized in Table I. The sequence collected 46 Cartesian partitions in the SI direction, covering three-fourths of k-space with 384 samples per line. The central partition was used to determine a gradient-delay correction by comparing lines acquired in opposite directions for the latter half of

the number of acquired spokes.^{20,32} The correction shifted acquired spokes by modulating their Fourier transform with a complex wave. After delay correction, the missing one-fourth of k-space was synthesized using a partial-Fourier projection-onto-convex-sets technique to produce 58 partitions.³³ The noise whitening transform determined from the calibration scan was then used to transform the coil signals into synthetic signals with independent and identically distributed noise.

2.C. Back projection with gridding

Each spoke was back projected into image space using gridding reconstruction with a 7-voxel-wide Kaiser-Bessel kernel with the grid oversampled by 37.5%.^{34,35} Full radial

density compensation was applied using a ρ -filter for each spoke. Complex images, $C_i(\mathbf{r}, t)$, from individual coils were combined using the estimated coil sensitivity profiles $S_i(\mathbf{r})$ to produce complex back-projection images with homogenous spatial sensitivity in phase and intensity,

$$P(\mathbf{r}, t) = \sum_i^n S_i^*(\mathbf{r}) C_i(\mathbf{r}, t) / \sum_j^n S_j^*(\mathbf{r}) S_j(\mathbf{r}), \quad (1)$$

where i is an index identifying each coil among all n coils, \mathbf{r} is the spatial position of a voxel and t is the time when a spoke was acquired. The resolution, voxel size, and position of the back-projection images was set to match those of corresponding DCE-MRI images reconstructed by vendor software on the scanner as listed in Table I. These vendor images used a slice resolution of 72.5% and a slice oversampling of 25% bringing the number of final slices to 64.

2.D. View sharing

To produce a tomographic image, several back-projected images can be combined by a weighted sum in \mathbf{k} -space through view sharing.³⁶ To produce a set of images that show the gradual change over time or breathing phase, view sharing can be efficiently implemented by sorting the n back projections with respect to e.g., time, t , and then element-wise multiplying the resulting array with a filter. To do this, a series of back-projected images $P(\mathbf{r}, t)$ in \mathbf{r} - t -space is transformed with the discrete Fourier transform to \mathbf{k} - f -space

$$\tilde{P}(\mathbf{k}, f) = \mathcal{F}_{(\mathbf{r}, t)}^{(\mathbf{k}, f)} P(\mathbf{r}, t) \quad (2)$$

where $\mathbf{r} = (r_x, r_y, r_z)^T$ are the voxel indices in the x , y and z directions, t is the sorted spoke index, $\mathbf{k} = (k_x, k_y, k_z)$ are the \mathbf{k} -space voxel indices and f is the frequency index along the sorted spoke dimension. To cover the entire field of view (FOV), the sampling density in \mathbf{k} -space should be at least one. Therefore, we used a Gaussian view-sharing filter along the spoke dimension

$$W(\rho, f) = \exp\left(-2\pi^2 \left(\frac{f}{n}\right)^2 \sigma_t^2(\rho) - \frac{\rho^2}{2\sigma_w^2}\right) \quad (3)$$

with a width, σ_t , that depended on the distance $\rho = \sqrt{k_x^2 + k_y^2}$ to the k_z -axis

$$\sigma_t(\rho) = \begin{cases} \sqrt{\left(\frac{\pi\rho}{\alpha}\right)^2 + \sigma_{\min}^2}, & \frac{\pi\rho}{\alpha} \leq \sigma_{\max} \\ \sigma_{\max}, & \frac{\pi\rho}{\alpha} \geq \sigma_{\max} \end{cases} \quad (4)$$

and a maximum width in \mathbf{k} -space determined by a Gaussian window with width

$$\sigma_w = \beta \frac{\alpha \sigma_{\max}}{\pi} \quad (5)$$

where σ_{\min} and σ_{\max} are the minimum and maximum temporal widths of the view-sharing filter, α is the angular undersampling factor and β is a factor allowing reconstruction at higher temporal resolution at the expense of stronger streak artifacts. Motivated by the benign aliasing artifacts caused by

angular undersampling and the possible gain in resolution previously shown³⁷ we chose an angular undersampling factor of $\alpha = 3$ and a resolution increase of $\beta = 2$ for this work. The data in \mathbf{k} - t -space, were padded along the t -dimension with zeros to avoid wraparound caused by the filter.

After filtering, the \mathbf{k} - f -space signal is transformed back into \mathbf{r} - t -space to produce the final image series

$$I(\mathbf{r}, t) = \frac{\left(\mathcal{F}_{(\mathbf{r}, t)}^{(\mathbf{k}, f)}\right)^{-1} W(\rho(\mathbf{k}), f) \tilde{P}(\mathbf{k}, f)}{\left(\mathcal{F}_{(t)}^{(f)}\right)^{-1} W(0, f) \tilde{Q}(f)} \quad (6)$$

where $\tilde{Q}(f) = \mathcal{F}_{(t)}^{(f)} Q(t)$ is the Fourier transform of an indicator function indicating if the data at timepoint t were acquired or zero-padded to avoid wraparound. The denominator ameliorates the boundary effect at the beginning and end of the scan that would otherwise reduce the intensity of the first and last few images. A more elaborate strategy to tackle the temporal boundary effect has been proposed for model-based reconstruction with nonperiodic boundary conditions.³⁸ The simpler method described above was chosen instead after considering the reconstruction method and the time from the start of scan to CA arrival in the liver (approx. 1 min).

2.E. Reconstructions without motion correction

The back-projected images, previously created, were combined into a time series without motion correction using $\sigma_{\min} = 5$, producing a temporal resolution (2σ) of 2 s at the center of \mathbf{k} -space. This temporal resolution has previously been found sufficient to represent CA uptake curves.^{15,20} An upper limit, $\sigma_{\max} = 144$, was selected to be large enough to allow maximum spatial resolution and resulted in a temporal resolution of 58 s at the periphery of \mathbf{k} -space. No additional tuning or sensitivity analysis of the parameters in this work was performed. When no or rigid motion correction is applied, some of the Fourier transforms in the back-projection algorithm and Eq. (2) can be cancelled. However, to ensure comparability with the motion-corrected reconstructions, this simplification was not done.

Due to the small temporal spacing between the reconstructed image volumes (0.16–0.26 s) only every fifth was kept resulting in 400 image volumes with a temporal spacing of 0.79–1.3 s and no motion correction (NMC).

In addition to the view-sharing reconstruction, vendor (VEN) images were used to benchmark the motion correction methods described below.

2.F. Motion modeling

In order to label spokes by breathing motion states, a motion signal was derived from an image time series with high temporal but lower spatial resolution. This time series was reconstructed with view sharing as described above but with $\sigma_{\min} = 2$ and $\sigma_{\max} = 5$. The resulting 2000 images were rigidly aligned with respect to a reference image in an arbitrary breathing state using a robust region-limited rigid-body

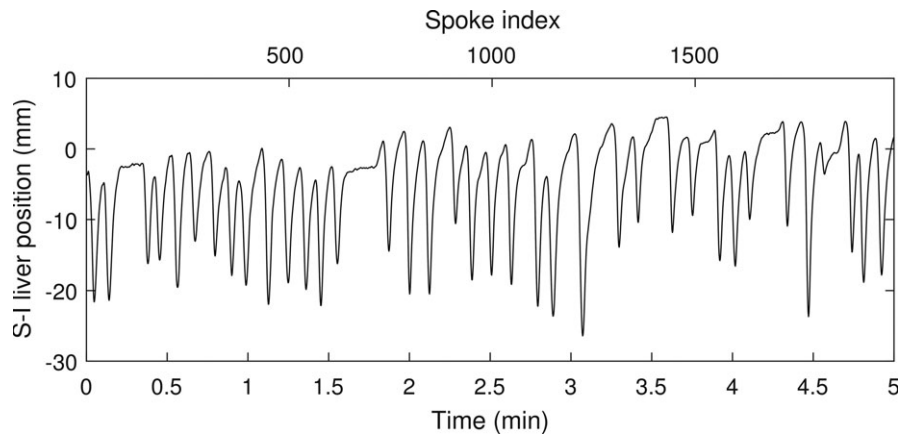


FIG. 2. An example of a patient motion signal showing the superior–inferior position of the liver during a 5-min scan. No effect on the motion signal from the contrast agent injected after 30 s is observed.

image registration algorithm¹⁴ with translation but no rotation. The reference image was selected among the VEN images by a physician. The superior–inferior (SI) translation, $s(t)$, of the center of mass of the liver was extracted from each of the 2000 transforms produced by the registration and used as a one-dimensional motion signal.²⁰ A sample motion signal for a subject can be seen in Fig. 2. No effect on the motion signal from the contrast agent, injected after 30 s, is observed suggesting that the rigid body registration was robust to changes in contrast.

The motion signal was used to sort the back-projections according to the position of the liver from inhale (smallest SI liver position) to exhale (largest SI liver position). Following sorting, the back-projections were combined using view sharing but with the motion signal as view-sharing dimension rather than time. For this reconstruction, σ_{\min} was set to 100 spokes and σ_{\max} to 200 spokes. Out of the 2000 resulting image volumes, 21 volumes, evenly distributed from the first to the last sorted spoke, were kept as representations of the breathing states from inhale to exhale.

The 20 nonexhale motion states were aligned within the whole field of view to the end-exhale state using a deformable image registration algorithm based on cubic B-spline deformations and a normalized mutual-information metric as implemented in the software package NiftyReg.³⁹ The grid spacing of the B-spline grid was $3 \times 3 \times 2$ pixels. The registration problem was regularized by adding the log of the Jacobian determinant as well as bending energy as penalty terms to the objective function with weights 0.8 and 0.005, respectively. The state closest to exhale was first aligned to the end-exhale state. The resulting deformation field was then used to initialize the registration process for the state second closest to exhale. The second deformation field was then used to initialize the third registration and so forth. In this way, each registration need only compensate for the small displacements between neighboring motion states while still registering each state to the exhale state to reduce error propagation that might otherwise result from serial registration of the states.

To allow comparison of deformable motion correction of the whole abdomen to local rigid-body motion correction of the liver, a rigid-body transform with rotation and translation was derived from the nonrigid-body deformation fields by least squares fitting of the coordinates of the voxels inside the liver. These rigid-body transforms were then used to produce a set of 21 rigid-body transformation fields, one for each motion state.

2.G. Back-projection deformation

The time-dependent patient motion signal was used as an index for interpolation of the deformation field centered around each of the 2000 spokes from the 21 deformation fields. As a result, a time-dependent deformation field, $T(\mathbf{r}, t)$, was produced that converted a voxel position in the exhale state into the voxel position of the same anatomical structure for a given time, t . This deformation field was then used to transform all back-projected images, $P(\mathbf{r}, t)$, into motion-corrected back projections, $P_{\text{def}}(\mathbf{r}, t)$, by deforming them to the exhale state using linear interpolation.

$$P_{\text{def}}(\mathbf{r}, t) = P(T(\mathbf{r}, t), t) \quad (7)$$

Compared to model-based reconstruction, this motion-correction strategy is a simplification²¹ but can provide a computational advantage and has been shown to work well when the deformation fields are approximately affine within the width of the coil-sensitivity profiles.²⁶

A second set of corrected back projections were created by the same procedure but using the rigid-body transformation fields instead of the nonrigid.

2.H. View sharing of motion-corrected back projections

After deformation, the motion-corrected back projections, $P_{\text{def}}(\mathbf{r}, t)$, were combined using view-sharing with $\sigma_{\min} = 5$ and $\sigma_{\max} = 144$ in the same way as for the time series

without motion correction producing 400 image volumes with deformable motion correction (DMC) and a temporal spacing of 0.79–1.3 s. Image and voxel size was the same as for the vendor-reconstructed images as listed in Table I. An image time series with rigid-body motion correction (RMC) was also created using the back projections transformed by the rigid-body transformation fields.

2.1. Evaluation

DMC and RMC were compared to NMC image time series. All these time series were also compared to the VEN image time series reconstructed by vendor software.

Time series were compared with respect to the maximum signal enhancements of the PVIF and the arterial input function (AIF). The peak PVIF was chosen because the intensity of the portal vein is particularly sensitive to motion due to its small size and strong contrast to surrounding tissue before and after contrast administration. The AIF is less sensitive to motion but may be distorted by RMC focusing on the liver. Peak PVIF and AIF amplitudes could therefore be reduced by motion or inaccurate motion correction.

Parameter maps of arterial and portal-venous perfusion where also estimated from reconstructed images for all patients using a dual-input single-compartment model.⁴⁰ Portal-venous perfusion can be used as an indicator of global and local liver function⁸ whereas arterial perfusion can help select subvolumes for boosting during radiation therapy.¹ Central-venous outflow was also estimated as part of the pharmacokinetic (PK) model, but is not presented because no clinical application for it is known. Perfusion maps with and without motion correction were compared inside the gross tumor volume (GTV) and the liver as a whole as well as a normal tissue volume (NTV) drawn inside the liver but away from the tumor region. For parameter estimation, images reconstructed for the first and last 8 s of the scan were omitted to avoid the effect of any residual temporal boundary effect and the initial approach to spoiled gradient-echo steady state.

In addition to the quantitative evaluation measures above, reconstructed images and perfusion maps are presented for a subset of patients to illustrate the effect of motion correction on lesion conspicuity and estimated perfusion values. Descriptive statistics of the estimated deformation fields are also given to reflect the size and variation of motion among patients. For this purpose, each deformation field $T(\mathbf{r}, t)$ was compared to the rigid-body transform that best approximated it inside the liver. We defined the residual displacements inside the liver to be the part of the total voxel displacements that cannot be represented by rigid-body motion.

3. RESULTS

The distance traversed in the SI direction by the liver center of mass, from end exhale to end inhale, varied among subjects from 8 to 46 mm with a median of 15 mm. In the left–right and anterior–posterior directions, the displacements were 2–10 mm and 3–35 mm, respectively, with medians of 4 and 8 mm.

The median of the magnitude of the residual nonrigid voxel displacements inside the liver varied from 1 to 6 mm among subjects with a mean of 2 mm. The 95th percentile of the residual displacement magnitude varied between 2 and 15 mm within the population with a mean of 7 mm. The minimum and maximum Jacobian determinant of the inhale deformation fields inside the liver was in the range 0.73–0.94 and 1.06–1.46, respectively.

Oscillations were observed for time–intensity curves in image time series with high temporal resolution as seen in Fig. 3. These oscillations were smoothed out by the wider view-sharing filter for NMC images but a bias was introduced into the curve instead. DMC images did not exhibit this bias, as the underlying intensity oscillations had been compensated for.

Table II shows the statistical comparison of AIF and PVIF peak amplitudes from the different reconstruction methods (DMC, RMC, NMC, and VEN). In addition, arterial and portal-venous perfusion was compared in three region of interest (ROI) for the four reconstruction methods. To avoid Type-I

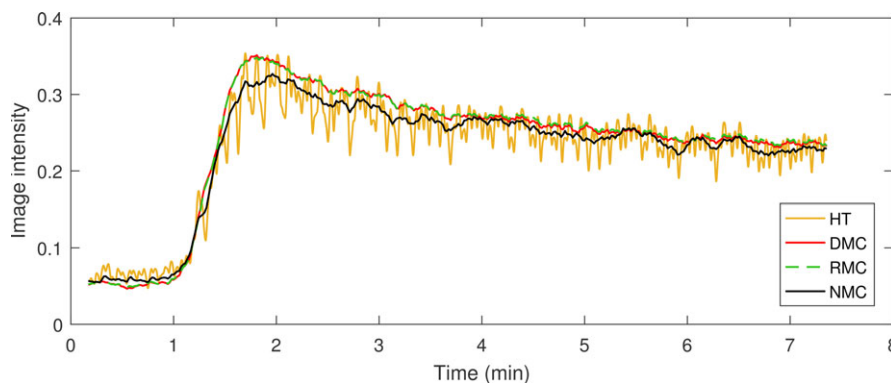


FIG. 3. Time–intensity curves for a PVIF ROI. Images reconstructed with high temporal resolution (HT) exhibit oscillations induced by breathing ($\sigma_{\min} = 5$ and $\sigma_{\max} = 10$). These oscillations are not visible for NMC and DMC images but do induce a bias for NMC images, as seen by the lower intensity compared to DMC images after CA administration. [Color figure can be viewed at wileyonlinelibrary.com]

TABLE II. *P*-values and confidence intervals (CI) for paired *t* test of the difference of the peak PVIF and AIF amplitude among reconstruction methods for all patients. Differences significant at a 0.1% level are indicated by asterisks and gray background.

Relative peak amplitude difference	PVIF		AIF	
	P-value	CI	P-value	CI
$(DMC - RMC)/((DMC + RMC)/2)$	1.19e-01	[-0.02, 0.01]	9.84e-01	[-0.02, 0.02]
$(DMC - NMC)/((DMC + NMC)/2)$	8.46e-07*	[0.03, 0.13]	1.24e-01	[-0.01, 0.03]
$(DMC - VEN)/((DMC + VEN)/2)$	1.92e-11*	[0.07, 0.16]	2.25e-17*	[0.11, 0.20]
$(RMC - NMC)/((RMC + NMC)/2)$	1.99e-07*	[0.04, 0.14]	2.75e-01	[-0.02, 0.03]
$(RMC - VEN)/((RMC + VEN)/2)$	1.09e-11*	[0.07, 0.17]	1.62e-16*	[0.11, 0.20]
$(NMC - VEN)/((NMC + VEN)/2)$	4.34e-02	[-0.02, 0.08]	4.03e-14*	[0.10, 0.20]

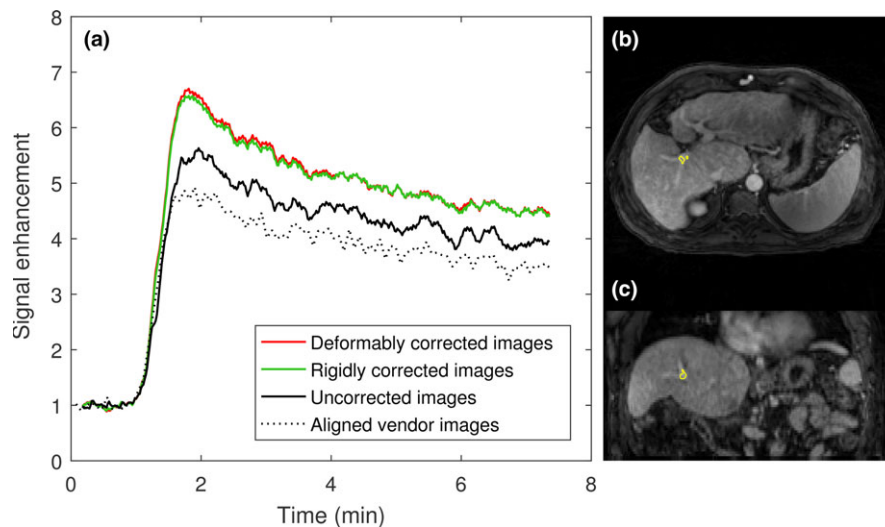


FIG. 4. (a) Portal-venous input functions with and without motion correction. The corresponding input function from images reconstructed by vendor software on the scanner is also shown. (b) and (c) show the ROI used to extract the PVIF. [Color figure can be viewed at wileyonlinelibrary.com]

errors due to multiple comparisons (48 in total), the significance level was Bonferroni-corrected from 5% to 0.1% for all tests and confidence intervals presented.

The peak amplitude of the PVIF was significantly higher for DMC and RMC images compared to NMC and VEN reconstructions with mean increases of between 8% and 12%. There was no significant difference in the peak PVIF amplitude between DMC and RMC. Sample PVIFs are shown in Fig. 4.

The peak amplitudes of AIFs did not differ significantly with and without motion correction. However, the peak amplitudes of the vendor AIFs were significantly lower than DMC, RMC, and NMC images because of the stronger aliasing in the precontrast vendor phases. Sample AIFs, extracted from the aorta of a subject at the branching of the celiac artery, are shown in Fig. 5

Mean arterial and portal-venous perfusion, k_a and k_p , in the GTV and the whole liver were significantly lower (Table III) in perfusion maps estimated from vendor images compared to those estimated from DMC, RMC, and NMC images. DMC and RMC reconstructions showed significantly lower portal-venous perfusion compared to NMC

reconstructions for the whole liver and GTV. Portal-venous perfusion did not differ significantly between DMC and RMC. There was no significant difference of the mean arterial perfusion in the liver between corrected and NMC images.

NMC perfusion maps showed artifacts primarily close to the edge of the liver. This effect was particularly severe for 11 of the 53 scans, as illustrated for an example patient in Fig. 6, where an area with falsely elevated arterial and lowered portal-venous perfusion is seen.

Three lesions from three separate patients are shown in Fig. 7 for DMC, RMC, and NMC reconstructions. Arterial perfusion is also shown for the DMC images. The DMC and RMC images are seen to have sharper lesion boundaries and internal structures than NMC. Aside from lesions, motion correction improved the sharpness of structures in the gastrointestinal (GI) tract as seen in Fig. 8. The changes over time in shape of the GI tract caused by peristalsis are seen more clearly in images with respiratory motion correction [Figs. 8(a) and 8(c)] than in those without [Figs. 8(b) and 8(d)] where the GI tract is blurred because of breathing motion.

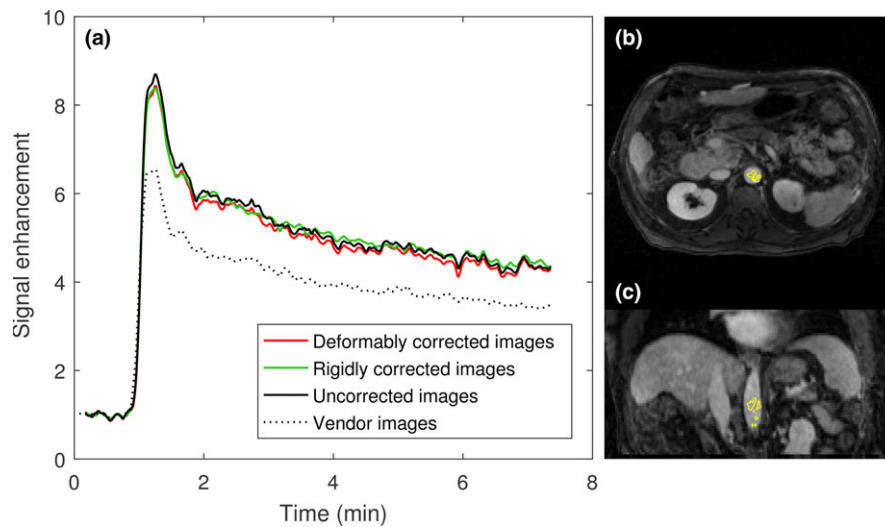


FIG. 5. (a) Arterial input functions from the aorta with and without motion correction. The corresponding input function from images reconstructed by vendor software on the scanner is also shown. (b) and (c) show the ROI used to extract the AIF. [Color figure can be viewed at wileyonlinelibrary.com]

TABLE III. Mean values and confidence intervals at the Bonferroni-corrected level of significance for differences in arterial and portal-venous perfusion for the different reconstruction methods. Significant differences are marked by asterisks and a gray background. All differences are given in ml/(100 ml·min).

	Portal-venous perfusion difference			Arterial perfusion difference		
	Whole liver	Normal tissue	GTV	Whole liver	Normal tissue	GTV
DMC-RMC	-0.1 [-2.2, 2.0]	0.5 [-3.0, 4.0]	0.3 [-3.0, 3.6]	-0.5 [-1.3, 0.3]	-0.6 [-2.1, 0.8]	-1.1 [-3.0, 0.9]
DMC-NMC	-7.8 [-13.3, -2.2]*	-8.9 [-18.7, 0.9]	-16.7 [-32.4, -1.1]*	-1.6 [-4.1, 0.9]	-0.2 [-3.3, 2.9]	1.3 [-4.1, 6.6]
DMC-VEN	54.6 [43.8, 65.4]*	66.8 [45.3, 88.3]*	41.0 [28.6, 53.4]*	8.6 [3.2, 13.9]*	5.3 [-1.2, 11.9]	19.9 [11.6, 28.1]*
RMC-NMC	-7.7 [-13.1, -2.3]*	-9.4 [-18.2, -0.5]*	-17.0 [-31.7, -2.4]*	-1.1 [-3.9, 1.6]	0.4 [-2.4, 3.2]	2.3 [-3.2, 7.9]
RMC-VEN	54.7 [43.6, 65.8]*	66.3 [44.8, 87.9]*	40.7 [28.8, 52.7]*	9.0 [3.7, 14.4]*	6.0 [-0.7, 12.6]	20.9 [12.7, 29.1]*
NMC-VEN	62.4 [51.5, 73.2]*	75.7 [52.9, 98.5]*	57.8 [40.5, 75.0]*	10.2 [4.3, 16.0]*	5.5 [-1.6, 12.6]	18.6 [10.8, 26.4]*

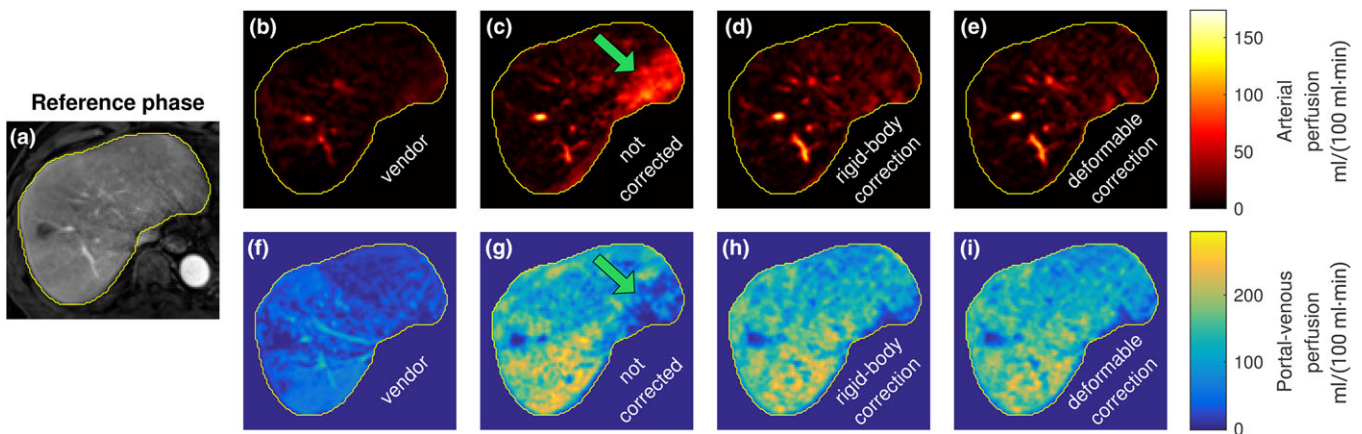


FIG. 6. The reference phase image used for delineation (a) as well as arterial (b–e) and portal-venous (f–i) perfusion parameter maps. Motion artifacts are indicated in the uncorrected maps (c, g) by the green arrow. [Color figure can be viewed at wileyonlinelibrary.com]

4. DISCUSSION

A method to perform respiratory DMC as part of image reconstruction for abdominal DCE-MRI has been presented and reconstructed images have been compared to those

reconstructed with RMC focused on the liver as well as to images without motion correction. DMC refocused the reconstructed MR images as evidenced by the increased peak amplitude of the PVIF but did not further increase the PVIF peak amplitude compared to RMC. As an effect of the

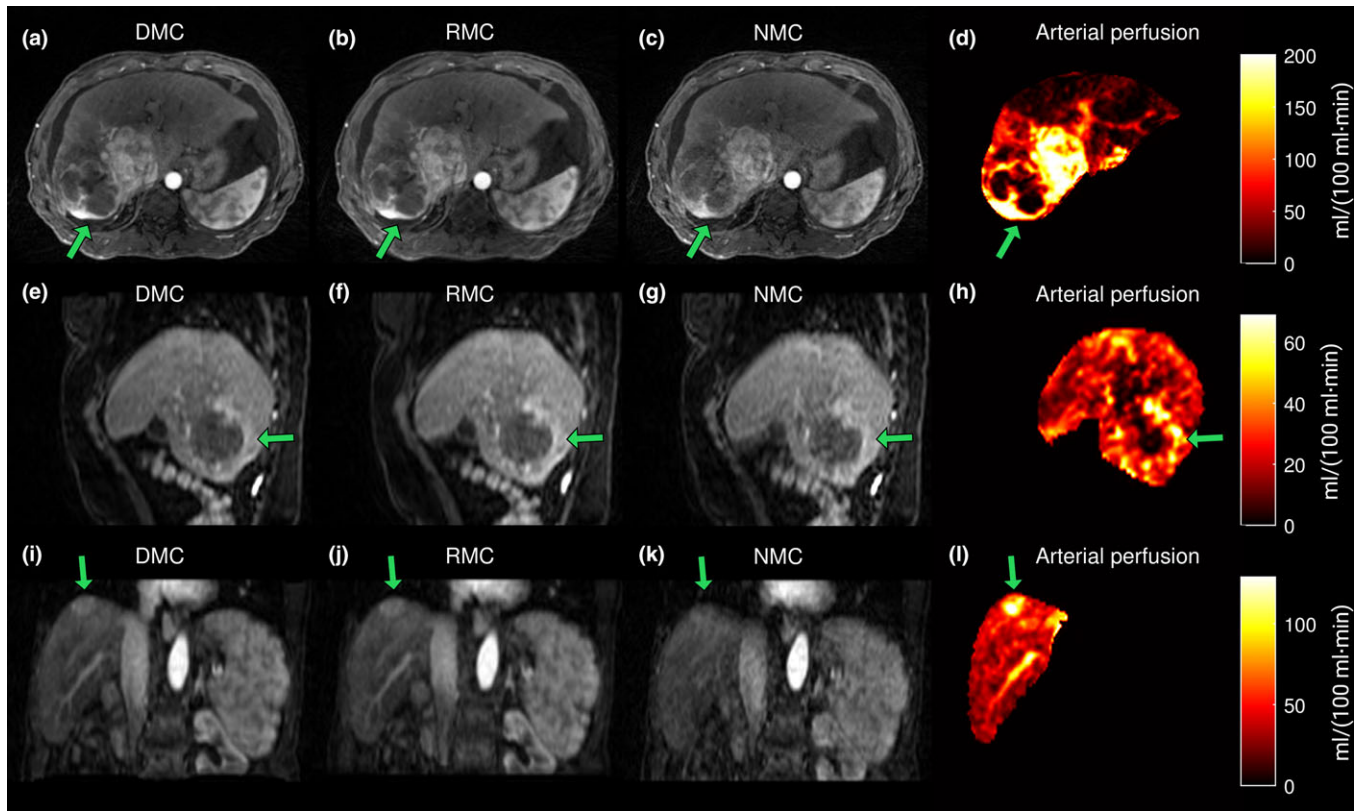


FIG. 7. Three tumors as they appear in images with deformable motion correction (a, e, i), with rigid-body motion correction (b, f, j) and without motion correction (c, g, k). The arterial perfusion maps produced from the DMC images are also shown. [Color figure can be viewed at wileyonlinelibrary.com]

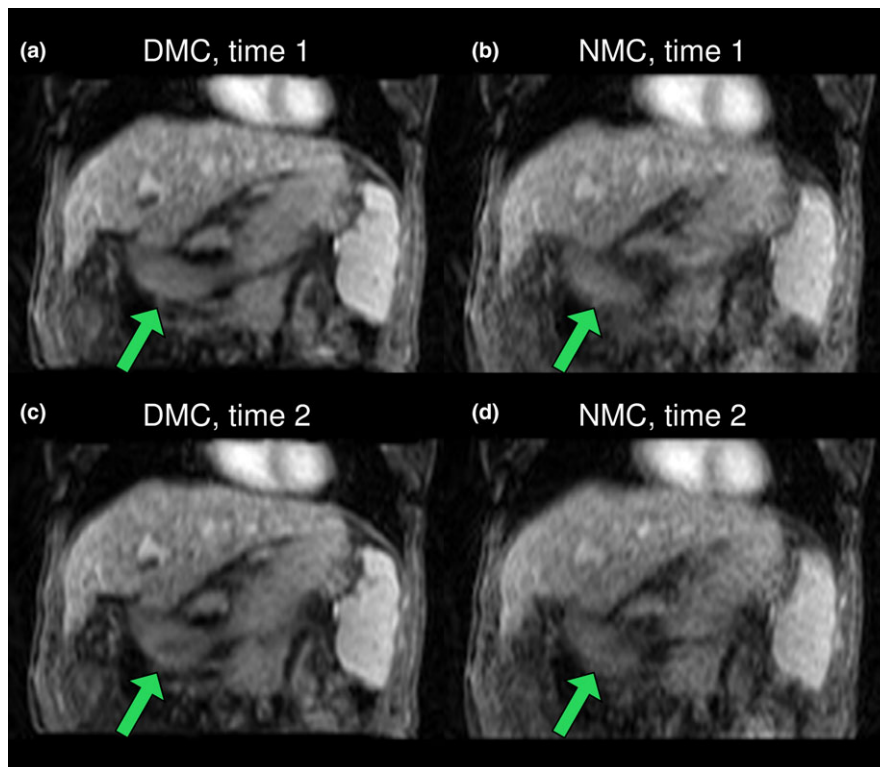


FIG. 8. The shape change of the gastrointestinal tract (arrow) over time, resulting from peristalsis is illustrated by two images at different time points corresponding to two separate peristaltic phases. The changes can be seen more clearly in the two images with deformable respiratory motion correction (a, c) than in images without motion correction (b, d). [Color figure can be viewed at wileyonlinelibrary.com]

increased PVIF, portal-venous perfusion was significantly lower in estimated perfusion maps.

Earlier studies have shown that increasing temporal resolution reveals strong respiratory oscillations in uptake curves in the liver.¹⁵ These oscillations can be counteracted by deformable alignment to produce smoother uptake curves. Our study supports this claim but also suggests that the additional improvement of image quality in the liver resulting from DMC is small compared to that already achieved by RMC.^{19,20} A benefit of correcting back-projection images for motion, as done in this study, rather than reconstructed images is that only the motion signal needs to have a high-enough temporal resolution to resolve the breathing cycles whereas the reconstructed time series only need to resolve the contrast-agent dynamics. This reduces the necessary frame rate for fast breathers. Another benefit of the presented method is that instead of using multiple affine transforms to correct the back projections from multiple coils,²⁶ one deformation field can be applied to a single coil-combined back-projection image, thereby reducing the number of transforms and complex images that must be stored and processed per time point.

The mean estimated portal-venous perfusion was higher in the liver for images without motion correction than in those with motion correction. This can be explained by the lower PVIF amplitude in images without motion correction, which is compensated for during parameter estimation by an apparent higher portal-venous perfusion.

Arterial and portal-venous perfusion maps estimated from vendor images were consistently lower than maps reconstructed with the presented view-sharing technique. This could be a consequence of the lower temporal resolution in the vendor images or the shape of the vendor view-sharing filter, which may introduce bias into the perfusion maps.

No deterioration of the AIF due to motion correction of the relatively stationary aorta was found. This was shown by the nonsignificant difference in AIF peak amplitude between motion corrected and noncorrected images. Rigid-body motion correction had no significant effect on the AIF, possibly because the main direction of liver motion is in the superior–inferior direction, producing a motion correction that has little effect on the aorta, which is oriented along the same axis. Vendor AIFs were significantly lower than all other reconstructions because of streak artifacts raising the intensity in the precontrast baseline.

For some subjects, motion correction was observed to eliminate regions of falsely high or low perfusion in estimated perfusion maps. These perfusion artifacts occurred primarily close to the high-contrast edge of the liver.

DMC did not improve input function extraction or perfusion estimation compared to RMC in this study despite residual nonrigid displacements. This can be understood by considering that (a) the aorta moves primarily along its own axis in the SI direction making MC unnecessary for the AIF, (b) the ROI of the PVIF is situated close to the center of the liver where RMC is sufficient to restore PVIF amplitude, and (c) the estimated perfusion maps are dominated by smooth

spatial variations that are only to a small degree affected by observed residual nonrigid displacements. DMC could still be of importance to enhance lesion conspicuity or to estimate spatially heterogeneous perfusion in bending liver lobes but no such case was observed in this study. It is also possible that a model-based motion-corrected reconstruction²¹ could reveal differences in estimated perfusion maps that the simplified method in this paper could not resolve.

A potential advantage of DMC over RMC is that it can correct for motion in multiple organs simultaneously, even when they are not moving in the same direction or with the same amplitude. Therefore, if uptake curves from multiple organs were needed, only one time series would have to be reconstructed, unlike rigid-body motion correction, which may require one time series per organ. However, the evaluation in this study is restricted to the liver and to a lesser extent the aorta, which is needed for hepatic perfusion estimation.

By correcting for motion, image blur can be counteracted such that liver and lesion borders can be seen more clearly. Therefore, motion correction may allow free-breathing scans to replace repeated-breathhold examinations as a basis for tumor delineation in the clinic. This finding agrees with earlier studies that demonstrated improved lesion sharpness using translational motion correction¹⁹ as well as higher quality scores given by radiologists to images reconstructed with parallel imaging to a higher temporal resolution¹⁵ thereby reducing motion artifacts. Improved image quality as determined by radiologists has also been demonstrated using golden-angle radial sparse parallel (GRASP) MRI¹⁸ to reduce motion artifacts by regularization in the temporal dimension.

A problem with deformable compared to rigid-body motion correction is the greater uncertainty in estimated transform parameters resulting from the registration of the respiratory motion states. For this study, deformable registration was regularized by bending-energy and Jacobian penalty terms. However, a compromise had to be made when selecting regularization parameters to accommodate the possible sliding interface of the liver, which may have resulted in overfitting of deformation fields inside the liver. Such overfitting could prevent accurate refocusing of internal liver structures.

By correcting for respiratory motion, peristalsis could be seen more clearly and this could aid the deformable registration of gastrointestinal motion. A cardiac motion signal would allow reconstruction of cardiac motion states and the construction of a cardiac motion model similar to the respiratory model presented in this work. By combining deformation vector fields from respiratory, cardiac, and gastrointestinal motion models, it would be possible to construct a comprehensive motion model and to correct for all three kinds of motion in the whole abdomen during image reconstruction. This is a focus of future research. Such a comprehensive motion model, tailored to the specific motion pattern of each patient, could aid image registration of other kinds of MRI and CT images as well as in target volume selection for radiation therapy or organ at risk

delineation. A comprehensive abdominal motion model could also be combined with CA-dependent MRI signal models to improve the accuracy and precision of estimated perfusion and uptake parameters.

5. CONCLUSIONS

Deformable motion correction applied to temporal image reconstruction can restore DCE-MRI uptake-curve amplitudes distorted by motion artifacts, improve the sharpness of lesion borders and internal structures and remove artifacts in perfusion parameter maps. However, no significant change in estimated perfusion was found for deformable motion correction as compared to rigid-body motion correction when restricting the evaluation to the liver.

ACKNOWLEDGMENTS

This work was supported by NIH/NCI P01 CA059827. The prototype Radial VIBE sequence was provided by Siemens Healthineers under a research agreement.

CONFLICTS OF INTEREST

The authors have no conflicts to disclose.

^{a)}Author to whom correspondence should be addressed. Electronic mail: ajohanss@med.umich.edu; Telephone: +1-734-936-3100.

REFERENCES

- Wang H, Farjam R, Feng M, et al. Arterial perfusion imaging-defined subvolume of intrahepatic cancer. *Int J Radiat Oncol Biol Phys.* 2014;89:167–174.
- Cao Y, Platt JF, Francis IR, et al. The prediction of radiation-induced liver dysfunction using a local dose and regional venous perfusion model. *Med Phys.* 2007;34:604–612.
- Simeth J, Johansson A, Owen D, et al. Quantification of liver function by linearization of a 2-compartment model of gadoteric-acid uptake using dynamic contrast enhanced magnetic resonance imaging. *NMR Biomed.* 2018;31:e3913, 1-15.
- El Naqa I, Johansson A, Owen D, et al. Modeling of normal tissue complications using imaging and biomarkers after radiation therapy for hepatocellular carcinoma. *Int J Radiat Oncol Biol Phys.* 2018;100:335–343.
- Cao Y, Pan C, Balter JM, et al. Liver function after irradiation based on computed tomographic portal vein perfusion imaging. *Int J Radiat Oncol Biol Phys.* 2008;70:154–160.
- Cao Y. The promise of dynamic contrast-enhanced imaging in radiation therapy. *Semin Radiat Oncol.* 2011;21:147–156.
- Cao Y, Wang H, Johnson TD, et al. Prediction of liver function by using magnetic resonance-based portal venous perfusion imaging. *Int J Radiat Oncol Biol Phys.* 2013;85:258–263.
- Wang H, Feng M, Jackson A, Ten Haken RK, Lawrence TS, Cao Y. Local and global function model of the liver. *Int J Radiat Oncol Biol Phys.* 2016;94:181–188.
- Motosugi U, Ichikawa T, Sou H, et al. Liver parenchymal enhancement of hepatocyte-phase images in Gd-EOB-DTPA-enhanced MR imaging: which biological markers of the liver function affect the enhancement? *J Magn Reson Imaging.* 2009;30:1042–1046.
- Katsube T, Okada M, Kumano S, et al. Estimation of liver function using T1 mapping on Gd-EOB-DTPA-enhanced magnetic resonance imaging. *Invest Radiol.* 2011;46:277–283.
- Nakamura S, Awai K, Utsunomiya D, et al. Chronological evaluation of liver enhancement in patients with chronic liver disease at Gd-EOB-DTPA-enhanced 3-T MR imaging: does liver function correlate with enhancement? *Jpn J Radiol.* 2012;30:25–33.
- Dahlqvist Leinhard O, Dahlström N, Kihlberg J, et al. Quantifying differences in hepatic uptake of the liver specific contrast agents Gd-EOB-DTPA and Gd-BOPTA: a pilot study. *Eur Radiol.* 2012;22:642–653.
- Zuo CS, Jiang A, Buff BL, Mahon TG, Wong TZ. Automatic motion correction for breast MR imaging. *Radiology.* 1996;198:903–906.
- Johansson A, Balter J, Feng M, Cao Y. An overdetermined system of transform equations in support of robust DCE-MRI registration with outlier rejection. *Tomography.* 2016;2:188–196.
- Chen Y, Lee GR, Wright KL, et al. Free-breathing liver perfusion imaging using 3-dimensional through-time spiral generalized autocalibrating partially parallel acquisition acceleration. *Invest Radiol.* 2015;50:367–375.
- Feng L, Axel L, Chandarana H, Block KT, Sodickson DK, Otazo R. XD-GRASP: golden-angle radial MRI with reconstruction of extra motion-state dimensions using compressed sensing. *Magn Reson Med.* 2015;75:775–788.
- Benkert T, Feng L, Sodickson DK, Chandarana H, Block KT. Free-breathing volumetric fat/water separation by combining radial sampling, compressed sensing, and parallel imaging. *Magn Reson Med.* 2017;78:565–576.
- Feng L, Grimm R, Tobias Block K, et al. Golden-angle radial sparse parallel MRI: combination of compressed sensing, parallel imaging, and golden-angle radial sampling for fast and flexible dynamic volumetric MRI. *Magn Reson Med.* 2014;72:707–717.
- Lin W, Guo J, Rosen MA, Hee KS. Respiratory motion-compensated radial dynamic contrast-enhanced (DCE)-MRI of chest and abdominal lesions. *Magn Reson Med.* 2008;60:1135–1146.
- Johansson A, Balter J, Cao Y. Rigid-body motion correction of the liver in image reconstruction for golden-angle stack-of-stars DCE MRI. *Magn Reson Med.* 2018;79:1345–1353.
- Batchelor PG, Atkinson D, Irarrazaval P, Hill DLG, Hajnal J, Larkman D. Matrix description of general motion correction applied to multishot images. *Magn Reson Med.* 2005;54:1273–1280.
- Odille F, Cindea N, Mandry D, Pasquier C, Vuissoz PA, Felblinger J. Generalized MRI reconstruction including elastic physiological motion and coil sensitivity encoding. *Magn Reson Med.* 2008;59:1401–1411.
- Grimm R, Früst S, Souvatzoglou M, et al. Self-gated MRI motion modeling for respiratory motion compensation in integrated PET/MRI. *Med Image Anal.* 2015;19:110–120.
- Fürst S, Grimm R, Hong I, et al. Motion correction strategies for integrated PET/MR. *J Nucl Med.* 2015;56:261–269.
- Cheng JY, Alley MT, Cunningham CH, Vasanawala SS, Pauly JM, Lustig M. Nonrigid motion correction in 3D using autofocusing with localized linear translations. *Magn Reson Med.* 2012;68:1785–1797.
- Vaillant G, Buerger C, Penney G, Prieto C, Schaeffter T. Multiple-region affine motion correction using localized coil sensitivities. *Proc Intl Soc Mag Reson Med.* 2011;19:4605.
- Block KT, Chandarana H, Milla S, et al. Towards routine clinical use of radial stack-of-stars 3D gradient-echo sequences for reducing motion sensitivity. *J Korean Soc Magn Reson Med.* 2014;18:87–106.
- Chandarana H, Block KT, Winfeld MJ, et al. Free-breathing contrast-enhanced T1-weighted gradient-echo imaging with radial k-space sampling for paediatric abdominopelvic MRI. *Eur Radiol.* 2014;24:320–326.
- Song HK, Dougherty L. k-Space weighted image contrast (KWIC) for contrast manipulation in projection reconstruction MRI. *Magn Reson Med.* 2000;44:825–832.
- Martini N, Santarelli MF, Giovannetti G, et al. Noise correlations and SNR in phased-array MRS. *NMR Biomed.* 2010;23:66–73.
- Brey WW, Narayana PA. Correction for intensity falloff in surface coil magnetic resonance imaging. *Med Phys.* 1988;15:241–245.
- Block KT, Uecker M. Simple method for adaptive gradient-delay compensation in radial MRI. *Proc Intl Soc Magn Reson Med.* 2011;19:2816.
- Cuppen J, van Est A. Reducing MR imaging time by one-sided reconstruction. *Magn Reson Imaging.* 1987;5:526–527.
- Jackson JI, Meyer CH, Nishimura DG, Macovski A. Selection of a convolution function for Fourier inversion using gridding. *IEEE Trans Med Imaging.* 1991;10:473–478.

35. Beatty PJ, Nishimura DG, Pauly JM. Rapid gridding reconstruction with a minimal oversampling ratio. *IEEE Trans Med Imaging*. 2005;24:799–808.
36. Bernstein MA, King KF, Zhou XJ. *Handbook of MRI Pulse Sequences*, 1st edn. Amsterdam; Boston: Elsevier Academic Press; 2004.
37. Peters DC, Korosec FR, Grist TM, et al. Undersampled projection reconstruction applied to MR angiography. *Magn Reson Med*. 2000;43:91–101.
38. Le M, Fessler JA. Efficient, convergent SENSE MRI reconstruction for nonperiodic boundary conditions via tridiagonal solvers. *IEEE Trans Comput Imaging*. 2017;3:11–21.
39. Modat M, Ridgway GR, Taylor ZA, et al. Fast free-form deformation using graphics processing units. *Comput Meth Prog Bio*. 2010;98:278–284.
40. Wang H, Cao Y. GPU-accelerated voxelwise hepatic perfusion quantification. *Phys Med Biol*. 2012;57:5601–5616.